ACTA IMEKO
ISSN: 2221-870X
June 2026, Volume 15, Number 2, 1 - 9

Novel sensor for the measurement of draft in mainsails

Antonio Affanni[1], Filippo Rupil[1], Francesco Trevisan[1]

[1] *Polytechnic Department of Engineering and Architecture, University of Udine, 33100 Udine, Italy*

ABSTRACT
The measurement of the actual shape of a sail during navigation is an important issue both for skippers and sail makers. Besides sophisticated optical approaches based on artificial vision or based on the use of fiber optics glued within a sail, we propose to directly measure the mainsail's draft by means of a full bridge strain gauge (specifically designed for this application on PCB) applied on the two sides of a fiber glass batten into an horizontal section of the sail. The proposed approach reveals to be accurate enough and has the benefits of a cheap implementation so that it can be used not only by racing yachts and sail makers but also by leisure yachts owners. Moreover, thanks to the wireless data transmission, the proposed system can be easily integrated in a network of multiple sensors completing in this way the set of navigation data.

Section: RESEARCH PAPER

Keywords: wind measurements; sail draft; PCB strain gauges

Citation: A. Affanni, F. Rupil, F. Trevisan, Novel sensor for the measurement of draft in mainsails, Acta IMEKO, vol. 15 (2026) no. 2, pp. 1-9. DOI: 10.21014/actaimeko.v15i2.2089

Section Editor: Francesco Lamonaca, University of Calabria, Italy

Received March 24, 2025; **In final form** January 13, 2026; **Published** June 2026

Corresponding author: Antonio Affanni, e-mail: antonio.affanni@uniud.it

1. INTRODUCTION

Even though the numerical modelling of a sail (both the main sail and/or a jib) of a sailing boat is quite a common practice among sail makers and boat designers [1], [2], in recent years the monitoring of parameters directly related to the actual shape of a sail during the navigation is becoming more and more appealing not only for racing yachts performance optimization but also for leisure yachts [3], [4].

Real time information on the actual shape of a sail during the navigation help the skipper to properly trim a sail, optimizing the pressure distribution on it thus maximizing the aerodynamic forces and eventually the boat speed; however, such information becomes crucial during overnight or poor visibility conditions of navigation.

Measurement systems based on cameras are quite used to address this issue [5]; they capture the position of tell-tails on the two sides of a sail or acquire the geometry of the leech of a sail or reconstruct the geometry of a prescribed colour marked cord. The drawback of such an approach relays on the susceptibility of the camera lenses to the operating conditions such as humidity, rain, poor illumination; moreover, the acquired images must be processed, by means of time-consuming algorithms so improving the complexity of this approach.

As an alternative, techniques based on the measurement of a physical quantity such as strain [6] or pressure distribution on the sail [7], [8] have been developed and implemented.

Moreover, a promising approach is based on fibre optic using a fibre Bragg grating onto the sail in order to measure temperature and strain from which it is possible to deduce information on the local curvature of the sail [9]. However, multiplexed optical sensors along the length of the chord are needed to detect different wavelengths of light for the multiple sensors sharing the same light and measurement system; thus, the hardware is not trivial and reveals to be expensive. In addition, an algorithm implemented into a dedicated processor is necessary to handle the acquired data in order to identify the curvature at given sections and, by interpolation and integration of curvatures, the shape of the chord is estimated; therefore, it results to be time consuming from the software point of view.

In this paper, we propose to directly measure the mainsail's draft by means of a full bridge strain gauge applied on the two sides of a fibre glass batten (possibly a full batten) firmly inserted into a pocket along a horizontal section of the sail. In this way, it is possible to deduce the local shape of the sail along a prescribed section by measuring the deformation of the corresponding batten. The developed sensor also accounts for the difference of temperature between the two sides of the sail and transmits data to a remote server via a WiFi connection, [10], [11], in order to perform a compensation of the thermal effects on the measurement of the sail draft.

Such a device has been designed to be low cost in order to be exploited not only by the racing teams but also by amateurs and

sail makers which can easily demonstrate an experimental matching between the simulated design performances of the sail and the actual ones during real navigation. Each of the alternative sensing methods (camera-based systems, pressure sensors, and optical fibre sensors) has its strengths and weaknesses compared to PCB-based strain gauges. PCB strain gauges are ideal for localized measurements at a low cost and are straightforward to integrate into systems, making them highly suitable for small-scale, cost-sensitive applications. Camera-based systems are great for full-field, non-contact measurements, particularly in dynamic or large-scale scenarios, but they require more complex setups and tend to be more expensive. Pressure distribution sensors offer good solutions for large area or force distribution measurements but are less precise in terms of localized strain. Optical fibre sensors offer the highest sensitivity and can be used for distributed strain sensing over long distances, but they require a more complex and expensive setup. For small, cost-sensitive applications, PCB-based strain gauges remain the most practical choice. Moreover, the design of the presented sensor is modular since along the batten length a number of such sensors can be placed so that the curvature under each sensor can be approximated to a local osculating circumference; in this way the curvature of the whole batten can be reconstructed even in the case of tapered battens typically used to move the maximum sagitta at a prescribed position.

Finally, such a device can be conceived as a black box to be placed in the region of the sail where the stress is expected to be high; in this way it will guarantee the sail maker from improper use of the sail outside the design operating specifications or guarantee conditions.

The paper is organized as follows. In section 2 the developed sensor based on strain gauges on PCB, the analogue front-end design, the temperature measurements, the microcontroller firmware, data transmission and the electronic board realization are described in detail.

Experimental results are presented in section 3 obtained by means of a bench realized for the acquisition of the deformation measurements, the analogue front-end characterization and the compensation of thermal effects.

2. SENSOR DESCRIPTION

This Section presents the design of the sensor for the measurement of mainsail's draft, whose block diagram is shown in Figure 1.

The sensing strain gauges realized on PCB (described in detail in Subsection 2.1) are glued to the mainsail batten's upwind and downwind faces, thus converting the draft information into a variation of resistance. The analogue front end (described in detail in Subsection 2.2) implements an amplified Wheatstone bridge, thus converting the strain gauge signals into a high-level voltage. The temperatures measurement block (described in detail in Subsection 2.3) uses three temperature sensors: two of them are mounted on each PCB half bridge and one is on the electronic acquisition board. The microcontroller firmware (described in detail in Subsection 2.4) acquires the analogue voltages (three temperatures and one deformation) and converts them into a 12 bit information; then, after having compensated the thermal effects, sends the data (through UART, 115.2 kbps) to the WiFi module which transmits the data to the server (either a laptop, a raspberry or a mobile phone) through TCP protocol. This way, the data of multiple measuring points can be easily extended to a network of sensors.

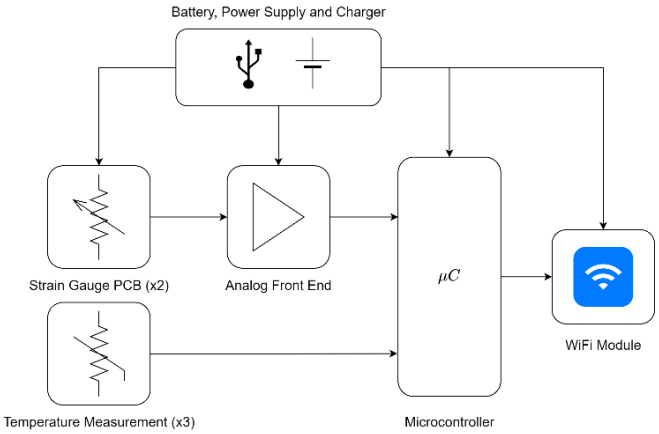

Figure 1. Block diagram of the proposed system.

The board is battery operated with a single 3.7 V, 850 mA·h LiPo cell, guaranteeing 10 hours of continuous data transmission; the battery is recharged through a micro-USB connector and a power management chip providing 500 mA in the constant current charge profile.

2.1. Strain Gauge design on PCB

The aim is to measure the deformation of a mainsail batten, by means of a strain gauges bridge, properly designed; with reference to Figure 2, we define the following geometrical quantities: r is the curvature radius of the batten's neutral axis, s is the sagitta, t = 5 mm is the batten thickness, l is the chord length, a is the length of neutral axis and φ is the corresponding central angle. The user specifications from the sail maker assumes a maximum batten deformation below 20 % of a; since the straight batten is long a = 2345 mm, the maximum sagitta (often denoted as camber) will be s_{MAX} = 469 mm. We then calculate the radius r of the circumference as

$$r = \frac{s}{2} + \frac{l^2}{8\,s}. \tag{1}$$

From r we then calculate the central angle φ as

$$\varphi = \frac{a}{r}. \tag{2}$$

Considering now the batten thickness t, the strain $\varepsilon = \delta l / l$ will then result

$$\varepsilon = \frac{\varphi\left(r \pm \frac{t}{2}\right) - a}{a}, \tag{3}$$

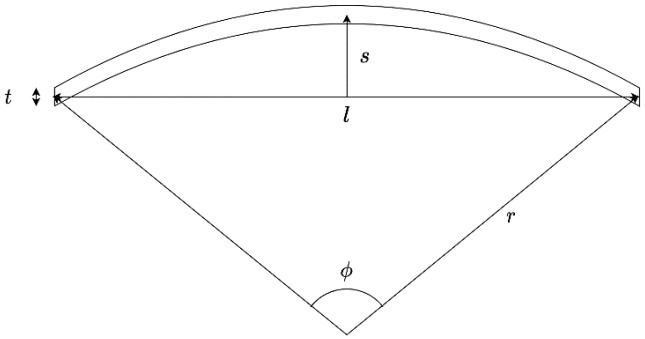

Figure 2. Geometrical quantities defining the batten curvature (pinned supports at the ends).

where ± denotes a stretch or a compression of the batten; for example, if the batten (see Figure 3) bends toward the top, the top face of the batten is stretched (+ sign in (3)) and the bottom face is compressed (-sign in (3)); with our geometrical parameters, the maximum strain results $\varepsilon_{MAX} = \pm 0.181$ %. We are aware that strain in the order of 2000 ppm is quite high and could give rise to non-linearity or hysteresis problems, however the batten thickness and material are designed by sail makers in order to achieve specific performances, thus we cannot override this constraint designing battens manifesting lower strain (e.g. thinner). Moreover, as shown in Section 3, the non linearity can be easily compensated in software.

Two PCBs (hereafter denoted as PCB "A" and "B") are glued to the mainsail batten top and bottom faces, as shown in Figure 3. To glue the PCBs to the two sides of the batten we used a specific glue, composed of hexamethylene diisocyanate homopolymer and ethyl acetate; this glue is specifically used in marine applications because it is particularly resistant to mechanical and environmental stresses. As drawback, on the other side, after curing it remains rubbery, thus potentially introducing non-linear or hysteretic behaviours. The curing of the glue consisted in four days rest at room temperature.

On each PCB face, a strain gauge is printed, thus obtaining four resistors, hereafter denoted as $R_{\mathrm{A,INT}}$, $R_{\mathrm{A,EXT}}$, $R_{\mathrm{B,INT}}$, $R_{\mathrm{B,EXT}}$ (Figure 3). When the batten bends (e.g. to the top direction), PCB A is stretched and PCB B is compressed; moreover, due to the thickness of the PCBs, $R_{\mathrm{A,EXT}}$ is strongly stretched, $R_{\mathrm{A,INT}}$ is weakly stretched and, dually, $R_{\mathrm{B,EXT}}$ is strongly compressed and $R_{\mathrm{B,INT}}$ is weakly compressed.

The PCBs have been designed with the same width of the batten and a length which assured a low cost (3 $/PCB) from the manufacturer, in 2 layers of metallization technology; also, the tracks of the pair of strain gauges have been designed for a low-cost application with 1 oz. copper. In Table 1 we report the strain gauges characteristics.

The track width has been set to 6 mils (≈ 0.152 mm) in order to maintain a low-price process and we arranged 92 turns of the serpentine for the overall length of the track 32.2 m. The theoretical rest resistance is 106 Ω. In Figure 4 it is shown the top view of the PCB, while the lower part of the Figure shows the strain gauge zoom close to the pads. On the bottom layer of the PCB there is an identical strain gauge, thus forming a half Wheatstone bridge; this explains the presence of three pads in Figure 4.

The single strain gauge resistance follows the equation

$$R_S = R_0[1 + (\beta(1 + 2\nu) + \alpha)(T - T_0)][1 + (1 + 2\nu)\varepsilon], \quad (4)$$

where R_0 represents the rest resistance, $\nu \approx 0.4$ is the Poisson's ratio, $\beta \approx 14$ ppm/K is the coefficient of thermal expansion (CTE) for PCB and glass fiber and $\alpha \approx 4000$ ppm/K is the thermal coefficient of resistance (TCR) for copper. Inserting the values obtained for the strain in (3), we expect a variation,

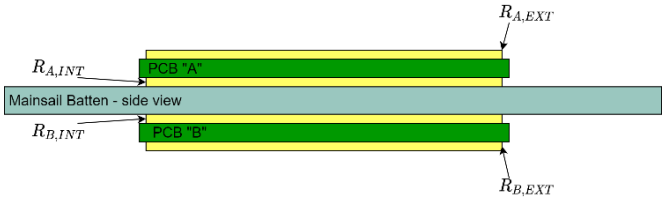

Figure 3. Side view of the batten with the PCB glued. Each PCB implements two strain gauges.

Table 1. Mechanical characteristics of the PCB-based strain gauges.

PCB Width	30 mm
PCB Length	350 mm
PCB Thickness	0.6 mm
Turns	92
Track Thickness	35 µm
Track Width	6 mils
Rest Resistance	106 Ω

roughly of ±0.35 Ω for $R_{\mathrm{A,INT}}$ and $R_{\mathrm{B,INT}}$; regarding $R_{\mathrm{A,EXT}}$ and $R_{\mathrm{B,EXT}}$, we have to use in (3) $t/2$+0.0006 in place of $t/2$, since the PCB is 600 µm thick, this means that we expect a variation of ±0.41 Ω on the external resistors.

However, the manufacturer declares a relative uncertainty on track width $u(W) = 20$ %; this introduces uncertainty on the quantity R_0 in (4) and we need to compensate it. To give an idea, we realized 15 PCB and we measured (with a 6.5 digits multimeter [12]) the values of R_0 shown in Table 2.

As shown in Table 2, even if the R_0 values are very different among different PCBs (in the order of 20 %), the half bridge of each PCB shows a deviation from the theoretical value of 0.5

Table 2. Resistance variability due to process uncertainty in PCB realization.

PCB	R_{TOP} (Ω)	R_{BOT} (Ω)	$R_{TOP}/(R_{BOT}+R_{TOP})$	Deviation %
1	86.126	84.938	0.496	0.3
2	95.268	100.065	0.512	-1.2
3	112.772	106.572	0.485	1.4
4	92.485	93.386	0.502	-0.2
5	114.295	107.735	0.485	1.4
6	105.813	100.723	0.487	1.2
7	109.992	102.021	0.481	1.8
8	108.934	112.009	0.506	-0.6
9	109.334	112.311	0.506	-0.6
10	95.147	90.286	0.486	1.3
11	92.528	92.772	0.500	-0.06
12	82.868	82.793	0.499	0.02
13	92.823	92.051	0.497	0.2
14	104.893	102.241	0.493	0.6
15	92.752	91.171	0.495	0.4

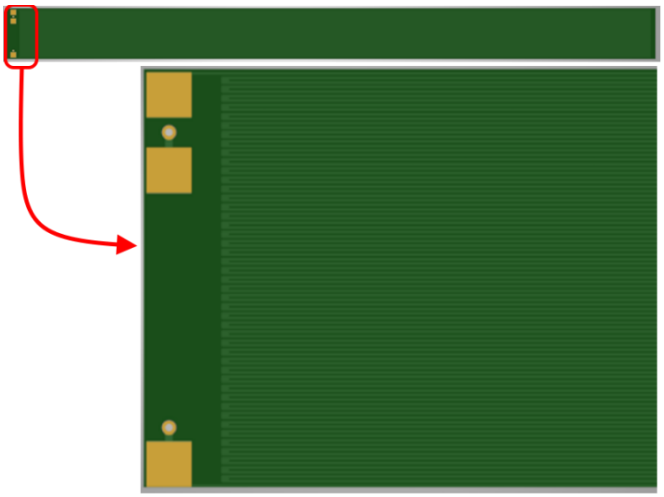

Figure 4. PCB realization of the strain gauges half bridge; top: the top view of the entire PCB; bottom: zoom of the pads zone. Note that three pads are shown, since one is common.

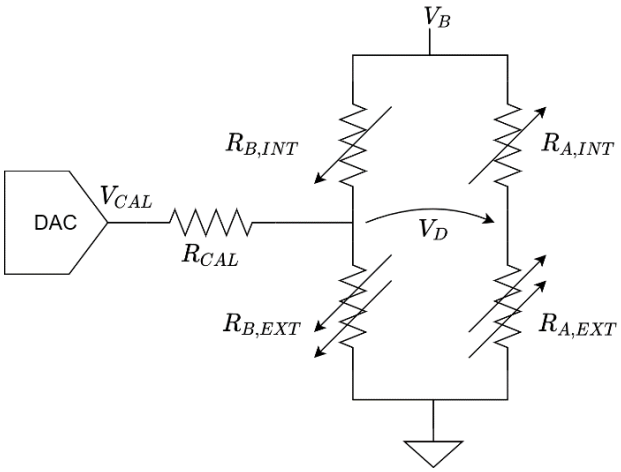

Figure 5. Bridge arrangement of the strain gauges. Double increasing arrow means high positive strain; single increasing arrow means low positive strain and dually for decreasing arrows.

which is in the order of 1.5 %; this deviation must be compensated in order to obtain the bridge balance.

Before describing the bridge arrangement, from (3) and Figure 3, one could argue that the best choice for the bridge arrangement (from the point of view of signal strength) would be one leg formed by $R_{\mathrm{A,B,EXT}}$ and the other leg composed by $R_{\mathrm{B,A,INT}}$, thus maximizing the strain imbalance; however, as will be discussed in Section 2.3, we observe that PCB A and B are on opposite faces of the sail and if one face is exposed to sun, the other will be in the shade, so the temperatures of PCB A and B will be different in most cases.

For the aforementioned reasons, we decided to design the bridge using each PCB as a leg of the bridge, as shown in Figure 5; in this case, the temperatures of the two strain gauges posed on each PCB will be very close each other, so the thermal effects in (4) are mostly self-compensated. In Figure 5 the increasing double arrow on the resistor means that the resistor has a strong increase (due to higher positive strain), the single increasing arrow means that the resistor has a weak increase (due to lower positive strain) and, dually for the decreasing double and single arrows with negative strains.

In Figure 5 the differential output voltage is marked as V_D and on the left we draw a DAC, on board the microcontroller, which generates the calibration voltage V_{CAL}, varying in the range [0, 3.3] V; we set $R_{\mathrm{CAL}} = 470\ \Omega$ assuring to compensate a variability of R_0 (in the same PCB, thus in the same leg) of 5 %.

2.2. Analogue Front-End Design

In this Subsection, we describe the circuit that converts the bridge imbalance into a high-level voltage to be acquired by the analogue to digital converter on board the microcontroller.

Figure 6 shows the schematic of the analogue front-end used to condition the signal. The expected variation of resistance calculated using (4) yields to have $V_{\mathrm{D}} \in$ [-1.7, 1.7] mV; moreover, we verified this interval experimentally, as will be discussed in Section 3.

The Instrumentation Amplifier used is MCP6N11 by Microchip [13], its transfer function is

$$V_{\mathrm{OUT}} = V_{\mathrm{REF}} + \left(1 + \frac{R_1}{R_2}\right) V_{\mathrm{D}}\,, \tag{5}$$

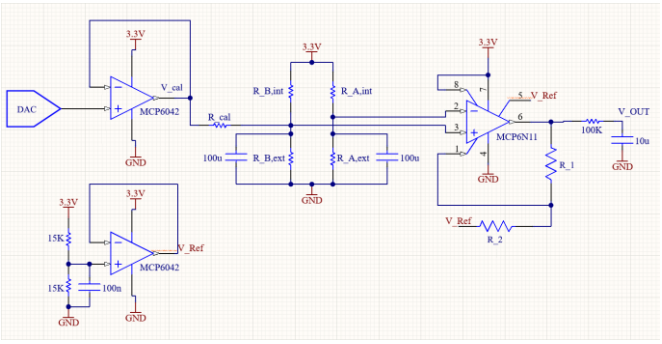

Figure 6. Schematic of the analogue front-end for the bridge signal conditioning.

where $V_{\mathrm{REF}} = 1.65$ V is the half range of power supply; choosing $R_1 = 330$ kΩ and $R_2 = 390\ \Omega$ we set the gain $G \approx 850$ in order to obtain $V_{\mathrm{OUT}} \in$ [0, 3.3] V. V_{REF} is obtained from a voltage divider (thus guaranteeing ratiometric behaviour) and a buffer realized using the operational amplifier MCP6042 by Microchip [14]. Similarly, the calibration voltage V_{CAL} is obtained from the DAC voltage passing through a buffer realized with an identical operational amplifier.

At the output voltage we implemented a passive, first order, anti-alias low-pass filter; this filter has a cutoff frequency of $f_{3\mathrm{Db}}$= 0.16 Hz; the sampling frequency is roughly ten times higher, $f_{\mathrm{S}} = 2$ Hz, as will be discussed in 2.4

2.3. Temperature Measurements

As stated in previous Section, the temperatures of the two half bridges and of the electronic board can be very different, since one face of the batten can be exposed to sun while the other is consequently in the shade. From (4), we observe that e.g. 30 °C of temperature variation yields to a variation of resistance of ≈ 12 Ω, by far higher than the change of resistance due to strain. Fortunately, the choice of arranging the bridge as two half bridges which lean on the same PCB, strongly reduces these thermal effects, since the PCB can be considered isothermal and the quantity $(\beta(1+2\nu)+\alpha)(T-T_0)$ in (4) does not play a role. Moreover, the thermal expansion β will act in the same way on each PCB, thus compensating the undesired thermal expansion effects on the bridge voltage. However, a residual difference of temperatures between the two sides of each PCB still may remain, so we decided to measure three temperatures: 1) on PCB A, 2) on PCB B and 3) on the electronic board.

To measure the temperatures, we used three negative temperature coefficient (NTC) thermistors, we recall that NTC has the temperature/resistance relation

$$R_{\mathrm{T}} = R_{298}\, \mathrm{e}^{B\left(\frac{1}{T}-\frac{1}{298}\right)}, \tag{6}$$

being T expressed in Kelvin and B is the characteristic temperature of the device. In our case we chose an NTC having $R_{298} = 10$ kΩ and $B = 3620$ K.

Since the NTC has a highly nonlinear behaviour, we decided to linearize the device by realizing a voltage divider as shown in Figure 7; the output voltage V_{OUT} is thus increasing with temperature in a quasi-linear behaviour, presenting an inflection point at the operating point T_{C}. In our case, we set the linearization point at $T_{\mathrm{C}} = 308$ K (i.e. 35 °C), assuming that normally the temperature on the sail $T \in$ [0, 70] °C; the voltage divider is formed by a second resistance R_{L},

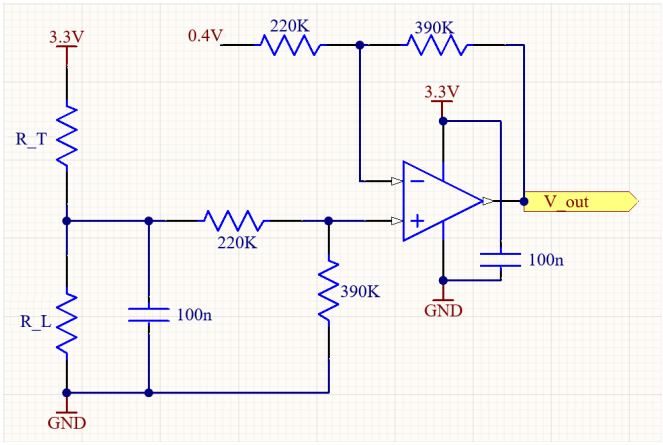

Figure 7. Schematic of each of the three temperature sensors signal conditioning. Left: linearization with voltage divider; right: voltage shift and amplification.

$$R_{\mathrm{L}} = R_{\mathrm{TC}} \frac{B - 2\,T_{\mathrm{C}}}{B + 2\,T_{\mathrm{C}}}, \tag{7}$$

where R_{TC} represents the NTC value at the temperature T_{C} . In our conditions, R_{L} = 4.7 kΩ. Since the voltage divider output V_{T} = 3.3 $R_{\mathrm{L}}/(R_{\mathrm{T}}+R_{\mathrm{L}})$ for $T \in$ [0, 70] °C varies in the range $V_{\mathrm{T}} \in$ [0.4, 2.3] V, in Figure 7 on the right we shift down the divider voltage by -0.4 V and amplify by a factor 390/220 ≈ 1.77 in order to obtain that the circuit generates 0 V when T = 0 °C and 3.3 V when T = 70 °C.

2.4. Microcontroller Firmware

The conditioned analogue signals (three temperatures and one deformation) shown in previous Subsections are acquired by the ADC on board the microcontroller. The chosen device is the STM32G0B1KET6 from ST Microelectronics [15]; the selected device has internal 12-bits ADCs and DACs and we set up the clock frequency f_{CK} = 16 MHz. As shown in Figure 8, at the startup the firmware checks if the user is pressing the switch for the calibration of R_0; if in the first 10 s the user does not press the switch, the microcontroller enters the operating cycle. In this cycle, an interrupt is set on a timer to raise every 500 ms; at the interrupt event, the firmware reads the three temperatures and the deformation signals, applies the thermal compensation and finally transmits the compensated data to the WiFi module. In case that the user presses the calibration switch (CAL key), the firmware starts iteratively changing the DAC output accordingly to the usual bisection algorithm and reading the ADC bridge values; when the bridge is balancing close to the center of the ADC span (i.e. 2048), the DAC stops searching and the last value of the DAC is stored on a non-volatile memory.

The temperature compensation algorithm is based on the results shown in Section 3.3; to implement it, we applied the superposition principle. We found the sensitivity of the output with respect to temperature changes in PCB A, PCB B and the electronic board; once we found the three sensitivities, we subtracted the thermal components using linear approximation. Naming the γ_A and γ_B the sensitivities of PCB A and PCB B respectively, we obtain the compensated signal V_{C} as

$$V_{\mathrm{C}} = V_{\mathrm{OUT}} - \gamma_{\mathrm{A}}\left(T_{\mathrm{A}} - T_{0,\mathrm{A}}\right) - \gamma_{\mathrm{B}}\left(T_{\mathrm{B}} - T_{0,\mathrm{B}}\right) \tag{8}$$

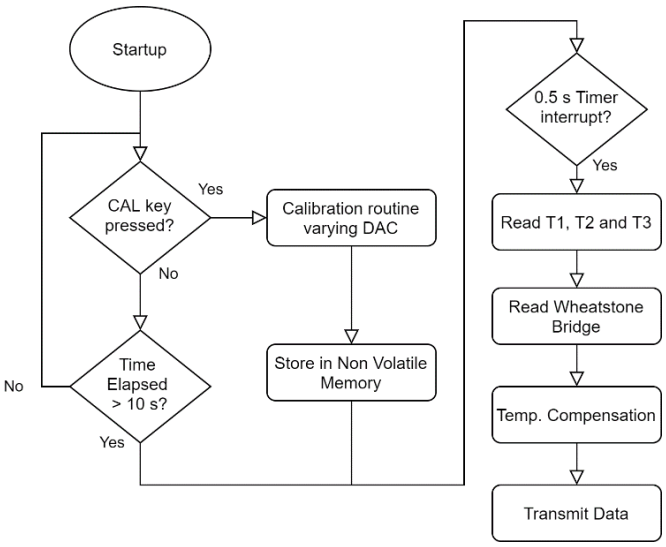

Figure 8. Flowchart of the firmware implemented in the microcontroller.

where $T_{0,\mathrm{A}}$ and $T_{0,\mathrm{B}}$ are the temperatures stored during calibration. Please note that the temperature of the electronic board does not enter in (8); in Section 3.3 we will show that the temperature of electronic board gives rise to negligible thermal effects.

Finally, the microcontroller transmits the compensated datum to the WiFi module using UART peripheral at baud rate 115.2 kbps.

2.5. Data transmission

The WiFi module that we chose is the USRC216 device by PUSR [16]. This module has the main advantage of low power operation, it consumes in fact only 60 mA during transmission; moreover, it can be easily configured, using a web page, in many different operating modes. In our setup, we decided that the module worked as access point and communicated with connected devices as a server using TCP protocol. In the future, we plan to use this sensor in a network of several measuring points, thus they will communicate with a single access point, in client mode, and probably using UDP protocol.

2.6. Electronic Board Realization

The schematic of the overall circuit is shown in Figure 9. The PCB has been realized using two layers PCB using SMD components; we have to notice that for passive components we chose 1206 package (120 × 60 mils) which is quite big compared to 0603 or 0402 packages. We chose this package in order to facilitate the manual soldering on the prototype, but we plan to move to smaller packages for production. The board is shown in Figure 10, its dimensions are 94 mm × 30 mm; the electronic components are placed only on the top layer, since we foresee to glue the electronic board to the batten.

In Figure 10 are evidenced the blocks described in previous Subsections.

3. EXPERIMENTAL RESULTS

In this Section, we present the experimental results obtained from our sensor, starting from the characterization of the strain gauges, passing through the analogue conditioning circuit, moving to the thermal behaviour and finally to the tests obtained on the entire system.

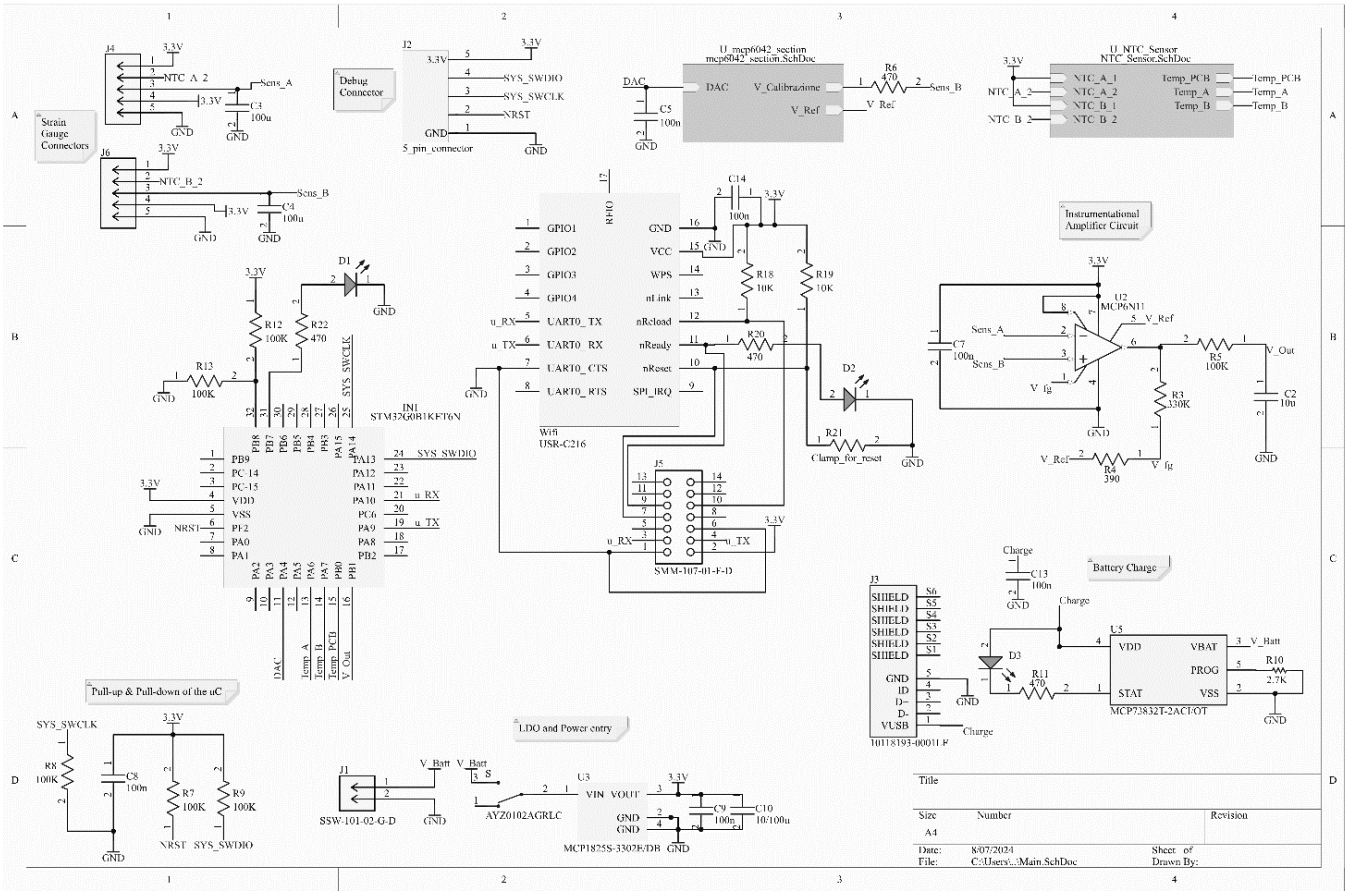

Figure 9. Schematic of the entire electronic board.

Before introducing the experimental results, we show (see Figure 11) the measurement bench that we built to characterize the sensor. In order to obtain repeatable measurements, we put on a desk a guide forcing the batten to nine fixed positions (besides the linear rest position) in order to have arcs with fixed chords and sagittas. Considering also the flipped batten, we could test the sensor in 19 fixed positions. For the sake of clarity, we point out that the 19 positions on the bench are not obtained by clamping the batten to the bench (which would yield to non-circular bending), but are obtained forcing the batten between two travel stops; this forms hinge supports which assure that the shape of the batten is a circular arc due to pure bending, as shown in Figure 11. Referring to equations (1), (2) and (3), we report in Table 3 the values of curvature (as percentage of batten length), sagitta s, chord length l, radius r, central angle ϕ and strains ε that we reproduced using the bench shown in Figure 11.

3.1. Strain gauges resistance

The values of resistance of the four strain gauge on the bridge have been logged using the data logger DAQ970A by Keysight technology [12]. It has on board a 6.5 digits converter with basic accuracy 0.003 %; in our conditions, we perform resistance measurements and the accuracy of the instrument results, from the manual, $u_B(R)$=11 mΩ. We set up a measurement procedure cycling the nine positions shown in Table 3 back and forth and also flipping the batten; this way, each cycle consisted of 38 positions. Each cycle was repeated four times and each position in the cycle was acquired by the logger ten times; summarizing, we acquired a total amount of $38 \times 4 \times 10 = 1520$ values for each strain gauge.

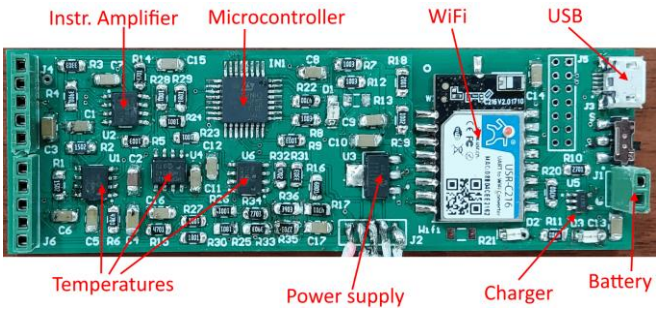

Figure 10. PCB realization of the electronic board. Text and arrows evidence the devices' description.

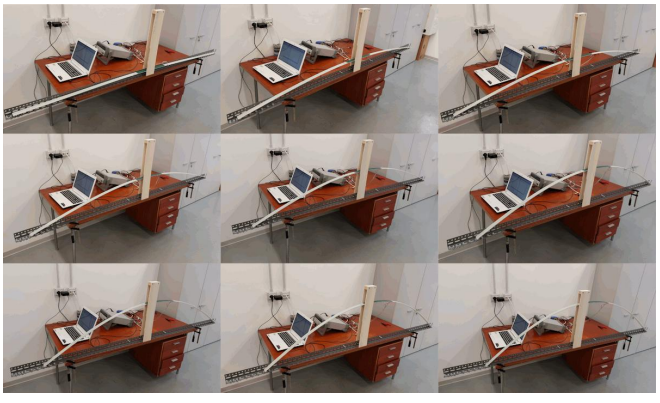

Figure 11. Bench realized for the acquisition of experimental results. The guide with nine fixed positions forces the batten at repeatable curvatures.

Table 3. Curvature, sagitta *s*, chord *l*, radius *r*, angle ϕ and strains ε set with the measurement bench.

Curvature %	*s* (mm)	*l* (mm)	*r* (mm)	ϕ (rad)	$\varepsilon_{A,B,INT}$	$\varepsilon_{A,B,EXT}$
0	0	2345	∞	0	0	0
1.7	40	2340	17131	0.136	±0.00014	±0.00018
4.9	115	2325	5933	0.395	±0.00042	±0.00052
7.5	177	2305	3840	0.610	±0.00065	±0.00080
9.8	230	2285	2952	0.794	±0.00084	±0.00105
12.5	295	2245	2283	1.027	±0.00109	±0.00135
14.9	350	2205	1911	1.226	±0.00130	±0.00162
16.8	395	2165	1681	1.395	±0.00148	±0.00184
18.7	440	2125	1503	1.560	±0.00166	±0.00206
20.2	475	2085	1382	1.697	±0.00181	±0.00224

In Figure 12 we show the values of the four strain gauges in each cycle; the error bars represent the standard deviation over the different cycles.

We observe that the imbalance of R_0 is higher than the measurement itself, so the calibration procedure shown in Sections 2.2 and 2.4 is mandatory. As second observation, we notice that the theoretical values of resistance variation calculated using (4) are close to the ones shown in Figure 12.

3.2. Analog front end characterization

Once realized the analogue front-end, we measured the performances of the amplified voltage by varying the positions on the bench. In a way similar to previous Subsection, we performed five cycles back and forth in the different positions and we acquired, with the same data logger as in previous Subsection, 10 samples per point, thus collecting a total number of $19 \times 5 \times 10 = 950$ samples.

Figure 13 shows the output voltage at the amplifier output as function of the sagitta's height; the blue trace represents the linear least squares interpolation. Looking at the graph, we must make some considerations:

- The behaviour looks hysteretic, the hysteresis can be quantified in 80 mV on V_{OUT}; in terms of sagitta's height it corresponds to 29 mm.
- The behaviour is non-linear; the non-linearity appears 170 mV on V_{OUT}; in terms of sagitta's height it corresponds to ±61 mm.
- The error bars represent the reproducibility of the measurements which can be quantified in 70 mV; in terms of sagitta's height it corresponds to 25 mm.

In Figure 14 we show the linearity error expressed in terms of sagitta's height which confirms the observations above.

In order to quantify the repeatability of the sensor at its central position, we iteratively turned on the circuit, measured 20 samples and then turned off the circuit. In Figure 15 we show the repeatability of V_{OUT} over ten cycles of turn-on and turn-off the circuit. We see that the repeatability is ±40 mV, corresponding to 14 mm of sagitta's height.

3.3. Compensation of thermal effects

In order to compensate the thermal effects on the measurement of the sail draft, we measured the variation of the output when the sensors were at the rest position, in a climatic chamber where we varied the temperature in the range [25 … 65] °C with steps of 10 °C. For convenience, since both bridge output and temperatures are acquired by the ADC, hereafter the values of temperature and of V_{OUT} will be expressed in terms of Least Significant Bits (LSB) of the ADC conversion; the compensation proposed in Section 2.4 uses directly these quantized values of temperature and V_{OUT}. For the sake of clarity, we point out that 1 LSB in temperature corresponds to 0.017 °C and 1 LSB on V_{OUT} corresponds to 805 µV (which, in turn, corresponds to 0.29 mm in sagitta's height).

In order to obtain the thermal sensitivity of each component, we applied the superposition principle by inserting in the oven:

- Only the PCB A sensor
- Only the PCB B sensor
- Only the electronic board

Figure 16 shows the behaviour of V_{OUT} in the three cases listed above, respectively; observing the graphs, we observe that, with a variation of 45 °C, PCB A gives rise to a positive drift of ≈+160 LSB (corresponding to 46 mm), PCB B gives rise to a negative drift of ≈ -220 LSB (corresponding to 63 mm) and the electronic board has negligible effects. We observe also that, as expected, the half bridge arrangement of strain gauges on the same PCB (discussed in Section 2.1) gives rise to quite small thermal drift; this drift includes the effects of both α (TCR) and β (thermal expansion) in (4). Moreover, as expected, their entity has similar magnitude and opposite sign (since they enter a differential amplifier).

In order to apply the calibration shown in (8) we used the numerical values $\gamma_A = 0.069$ and $\gamma_B = -0.094$.

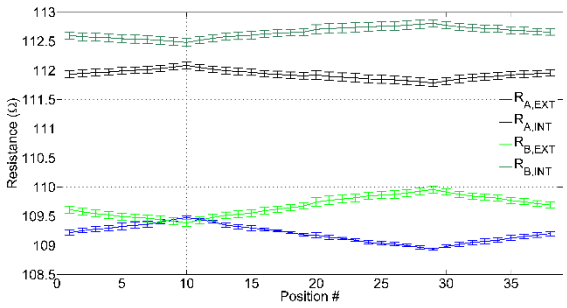

Figure 12. Strain gauges values measured using the bench in Figure 11; error bars represent the standard deviation over 4 cycles, 10 samples per measuring point in each cycle.

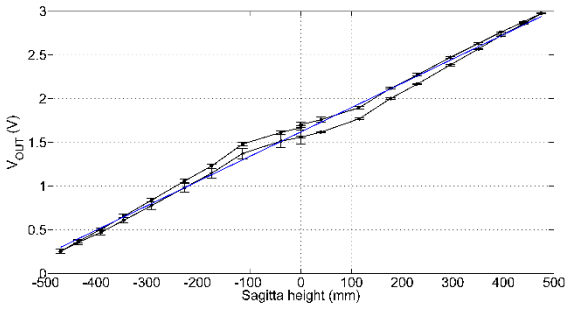

Figure 13. Conditioned output voltage varying the positions on the bench; error bars represent the standard deviation over 5 cycles, 10 samples per measuring point in each cycle. Blue line represents the linear least squares fitting.

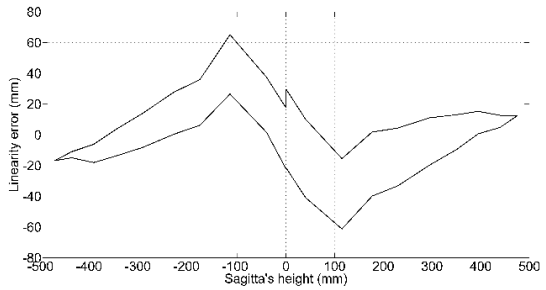

Figure 14. Linearity error (expressed in terms of sagitta's height) of the sensor readout.

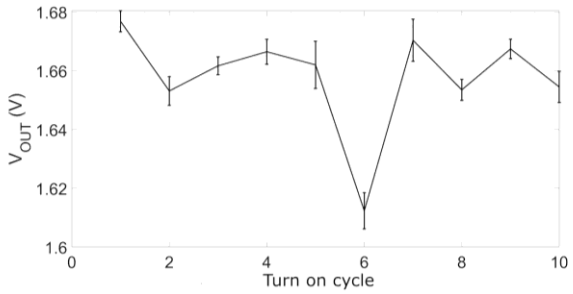

Figure 15. Repeatability test on the output voltage after the circuit turn-off/turn-on. Each error bar refers to 20 samples.

In order to verify the goodness of the applied compensation, we put the entire system in the climatic chamber, and we quantify the thermal drift after compensation. In Figure 17 we observe that the thermal drift is lower than 50 LSB, which corresponds to 14 mm of the batten camber.

3.4. Discussion

The proposed sensor accuracy is substantially comparable with the one obtained from Bragg grating fibres in [6], where the authors calculated an error in camber estimation in the order of 40 mm. Compared to the VSPARS system instead [5] the proposed sensor shows slightly worse performance, since the authors declare camber estimation error 0.5 % of batten length (i.e. 12 mm on our batten 2345 mm long). However, we recall that the proposed system has the advantages of being very low cost, easy to install on the sail and without connection cables thanks to wireless transmission.

The main limitation that we see in the proposed sensor is that the non-linearity that we observed is quite high, resulting about 61 mm in terms of sagitta's height; however, we observe that it can be easily compensated in firmware: thanks to the high repeatability, a compensation through look-up table can potentially reduce the non-linearity down to 25 mm in terms of sagitta's height. In Table 4 we summarize the performances of the proposed system compared to the state of the art using different methodologies.

Table 4. Performance comparison with the state of the art.

	Ref [5]	Ref [6]	This paper
Method	Cameras	Bragg fibres	PCB strain gauge
Setup	Easy	Complex	Easy
Cost	High	High	Low
Tough conditions	No	Yes	Yes
Processing	Demanding	Light	Light
Non-Linearity	12 mm	40 mm	61 mm
Modularity	High	Low	High

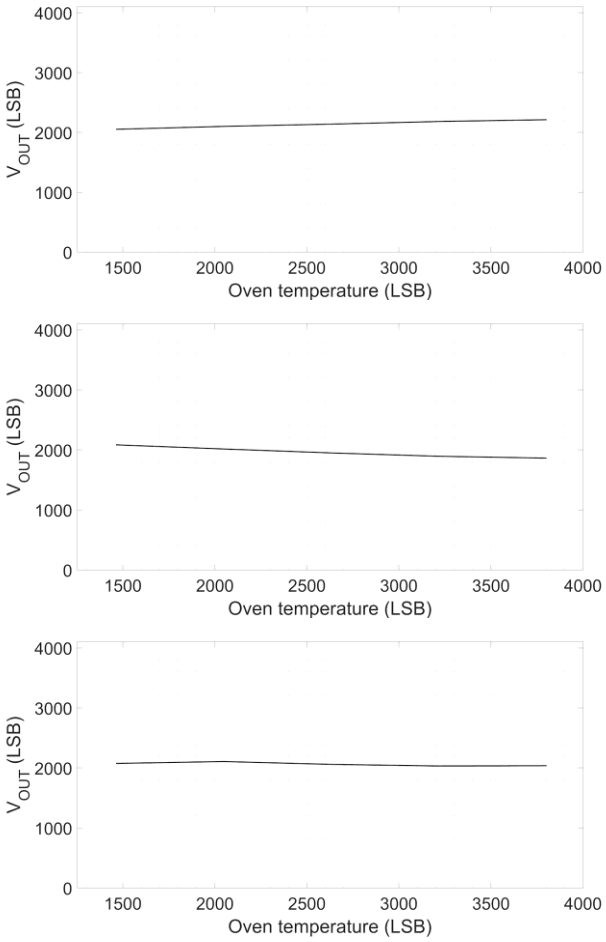

Figure 16. Top: thermal drift due to PCB A in the climatic chamber. Middle: thermal drift due to PCB B in the climatic chamber. Bottom: thermal drift due to the electronic circuitry in the climatic chamber.

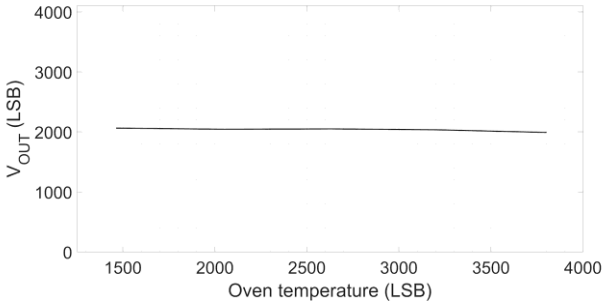

Figure 17. Sensor output, after thermal compensation, varying the temperature of the entire system. Thermal drift is 50 LSB, corresponding to 14 mm of the batten camber.

4. CONCLUSIONS

Measuring sail shape in real-time has proven to be particularly useful for optimizing the performance of sailing boats. Continuous monitoring of the curvature and deformation of the sails allows the crew to adjust them precisely, maximizing speed and enhancing control of the boat in particular during poor visibility conditions.

The proposed system consists of an electronic board that reads and conditions the signals from a resistive bridge made up of two pairs of strain gauge sensors, realized on *ad hoc* PCBs; the

properly conditioned data are then digitized and transmitted in real-time through Wi-Fi. This approach offers numerous advantages over existing alternatives, including ease of installation (battery-powered with wireless communication) and cost reduction, eliminating the need for optical interrogators or cameras. Additionally, the system incorporates temperature sensors for thermal compensation, improving the reliability of measurements even in variable environmental conditions.

Another improvement of the system in terms of linearity consists of trying different glues, since the cured glue that we used remains quite rubbery thus introducing additional non-linearity and hysteresis.

The implemented prototype, based on the results obtained, is an encouraging starting point for the development of a more comprehensive system that integrates and uses various units of the developed modules, creating a real-time map for sail shape reconstruction.

AUTHORS' CONTRIBUTION

Investigation, A. A., F. R. and F. T.; Validation, A. A., F. R. and F. T.; Writing – original draft, A. A., F. R., and F. T. All authors have read and agreed to the published version of the manuscript.

REFERENCES

[1] M. Lombardi, N. Parolini, A. Quarteroni, G. Rozza, Numerical simulation of sailing boats: dynamics, FSI, and shape optimization; Buttazzo, G., Frediani, A. (Eds.) Variational Analysis and Aerospace Engineering: Mathematical Challenges for Aerospace Design.. Springer, New York, 2012; pp. 339–378. DOI: 10.1007/978-1-4614-2435-2_15

[2] I. Viola, Recent advances in sailing yacht aerodynamics. Applied Mechanics Reviews 2013, 65, pp. 1–12. DOI: 10.1115/1.4024947

[3] I. M. Viola, R. G. Flay, Force and pressure investigation of modern asymmetric spinnakers. Transactions of the Royal Institution of Naval Architects Part B: International Journal of Small Craft Technology 2009, 151, pp. 31–40. DOI: 10.3940/rina.ijsct.2009.b2.98

[4] I. M. Viola, R. G. Flay, Sail pressures from full-scale, wind-tunnel and numerical investigations. Ocean Engineering 2011, 38, pp. 1733–1743. DOI: 10.1016/j.oceaneng.2011.08.001

[5] D. Pelley, O. Modral, VSPARS: a combined sail and rig shape recognition system using imaging techniques, Proc. of the 3rd High Performance Yacht Design Conf., Auckland, New Zealand, 2-4 December 2008; pp. 57–67.

[6] P. Ferreira, E. Caetano, P. Pinto, Real-time flying shape detection of yacht sails based on strain measurements. Ocean Engineering 2017, 131, pp. 48–56. DOI: 10.1016/j.oceaneng.2016.12.015

[7] A. Affanni, L. Casarsa, I. Scagnetto, F. Trevisan, Acquisition and integration of differential pressure measurements on sails for boat performances improvement, Acta IMEKO 12 (2023) 4, pp. 1–8. DOI: 10.21014/actaimeko.v12i4.1555

[8] F. Bergsma, D. Motta, D. Le Pelley, P. Richards, R. Flay, Investigation of sailing yacht aerodynamics using real time pressure and sail shape measurements at full scale, Proc. of the 18th Australasian Fluid Mechanics Conf., Launceston, Australia, 3–7 December 2012; pp. 473–476.

[9] J. Guemes, J. Menéndez, Response of Bragg grating fiber-optic sensors when embedded in composite laminates. Composites Science and Technology 2002, 62, pp. 959–966. DOI: 10.1016/S0266-3538(02)00010-6

[10] I. Scagnetto, G. Brajnik, P. Gus, F. Trevisan, Oceanus: a context-aware low-cost navigation aid for yacht racing. Journal of Navigation 2021, 74, pp. 738–749.

[11] M. De Piante, M. Midrio, R. Rinaldo, I. Scagnetto, R. Specogna, F. Trevisan, Sub-Gigahertz Path Loss Measurement Campaign in Marine Environment: A Case Study. Sensors 2024, 24, 2582. DOI: 10.3390/s24082582

[12] Keysight Technologies. DAQ970A/DAQ973A Data Acquisition System. Online [Accessed 20 September 2024] https://www.keysight.com/it/en/assets/7018-06259/technical-overviews/5992-3168.pdf

[13] Microchip Technology. MCP6N11. Online [Accessed 20 September 2024] https://www.microchip.com/en-us/product/MCP6N11

[14] Microchip Technology. MCP6042. Online [Accessed 20 September 2024] https://www.microchipdirect.com/product/MCP6042-I%2FSN ST Microelectronics. Mainstream Arm Cortex-M0+ 32-bit MCU, up to 512KB Flash, 144KB RAM, 6x USART, timers, ADC, DAC, comm. I/Fs, 1.7-3.6V. Online [Accessed 20 September 2024] https://www.st.com/en/microcontrollers-microprocessors/stm32g0b1ke.html

[15] PUSR Inc. SMT WiFi Module USR-C216. Online [Accessed 20 September 2024] https://www.pusr.com/products/low-power-iot-wifi-module.html